Published in final edited form as:
J Magn Reson. 2008 August ; 193(2): 274–285. doi:10.1016/j.jmr.2008.05.016.

An Open-Access, Very-Low-Field MRI System for Posture-Dependent ^{3}He Human Lung Imaging

L. L. Tsai[a,b,c], **R. W. Mair**[a,*], **M. S. Rosen**[a,d], **S. Patz**[c,e], and **R. L. Walsworth**[a,d]

[a]Harvard-Smithsonian Center for Astrophysics, Cambridge, MA 02138

[b]Harvard-MIT Division of Health Sciences and Technology, Cambridge, MA 02139

[c]Harvard Medical School, Boston, MA 02115

[d]Department of Physics, Harvard University, Cambridge, MA 02138

[e]Department of Radiology, Brigham and Women's Hospital, Boston, MA 02115

Abstract

We describe the design and operation of an open-access, very-low-field, magnetic resonance imaging (MRI) system for *in-vivo* hyperpolarized ^{3}He imaging of the human lungs. This system permits the study of lung function in both horizontal and upright postures, a capability with important implications in pulmonary physiology and clinical medicine, including asthma and obesity. The imager uses a bi-planar B_0 coil design that produces an optimized 65 G (6.5 mT) magnetic field for ^{3}He MRI at 210 kHz. Three sets of bi-planar coils produce the *x*, *y*, and *z* magnetic field gradients while providing a 79-cm inter-coil gap for the imaging subject. We use solenoidal *Q*-spoiled RF coils for operation at low frequencies, and are able to exploit insignificant sample loading to allow for pre-tuning/matching schemes and for accurate pre-calibration of flip angles. We obtain sufficient SNR to acquire 2D ^{3}He images with up to 2.8 mm resolution, and present initial 2D and 3D ^{3}He images of human lungs in both supine and upright orientations. ^{1}H MRI can also be performed for diagnostic and calibration reasons.

Keywords

hyperpolarized noble gas; low magnetic field; magnetic resonance imaging; lung imaging; open access

1 Introduction

In recent years, magnetic resonance imaging (MRI) of inhaled, hyperpolarized noble gas (^{3}He and ^{129}Xe) [1,2] has become a powerful method for studying lung structure and function [3, 4]. This technique has been used with conventional, clinical MRI instruments to make quantitative images of human ventilation [5,6], to acquire ^{3}He diffusion maps that yield images of lung gas-space dimensions [7,8], and to map the spatial variation of ^{3}He T_1 relaxation to provide images of alveolar O_2 concentration [9,10], which has recently been directly linked to the physiologically relevant ventilation/perfusion ratio (*V*/*Q*) [10]. Imaging of

*Corresponding author. Email: rmair@cfa.harvard.edu.

hyperpolarized ^{3}He has also found wide applications in the study of many lung diseases, including emphysema [11,12], cystic fibrosis [13] and asthma [14,15]. In all these clinical studies, subjects have been imaged while horizontal, generally supine, due to the design of clinical MRI systems based on a solenoid magnet with narrow inner diameter.

Numerous studies have investigated the effects of posture on pulmonary ventilation and perfusion [16–22], however these studies all gave global measures of the influence of posture and were incapable of providing regional information. Imaging techniques have been explored in recent times to try and overcome this limitation. Single-photon-emission computed tomography (SPECT) al-lows subjects to inhale tracers while vertical, however, subjects must still be positioned horizontally prior to imaging [23–25]. ^{3}He MRI has shown posture-related effects on lung volume even within the confines of a clinical MRI scanner: variable tissue compression and alveolar size variation has been observed via ^{3}He diffusion measurements as a function of subject orientation (prone, supine, left and right decubitus) [26]. Positron emission tomography (PET) has been used to directly measure ventilation and pulmonary perfusion [27,28], however, like in a clinical MRI scanner, subjects can only be imaged while prone or supine, and the restricted space prevents many diseased subjects or those with disabilities from being imaged.

An open-access system allowing MRI while the subject is in different body orientations and postures, including vertical, can have a variety of beneficial effects for the subject, and also provide important physiological information [29–31]. For pulmonary physiology in particular, there is a need for non-invasive mapping of the regional distribution of ventilation and perfusion as a function of body orientation and posture [16–20,32–35]. Additionally, significant questions relating to the care and survival of patients with severe lung diseases such as asthma or acute respiratory distress syndrome relate to postural effects [21,22,36] that an open-access lung MRI could help address. As obesity becomes a national health concern, studying the effect of increased body mass on ventilation, perfusion and lung volume also becomes vital [37], and would be better enabled by an open-access lung MRI. The need for open-access imaging of lung function has recently also been recognized by the Iowa Comprehensive Lung Imaging Center at the University of Iowa, which has announced a collaboration with Siemens Medical Systems to produce a novel vertically-oriented, open, low-field (~ 0.1–0.2 T) MRI system for this same purpose [38].

The advances in pulmonary MRI using inhaled ^{3}He and ^{129}Xe have been enabled by the high nuclear spin polarization, > 10 %, obtainable from laser-based optical pumping methods [1, 2]. This enhanced polarization, which can be ~ 10,000 times greater than that obtained via thermal equilibrium at 1 T, yields a magnetization of the same order as that found in water when placed in a large magnetic field. Furthermore, as the noble gas spins are polarized via the optical procedure prior to imaging, a large applied magnetic field, B_0, is not required for high-resolution MRI [39,40]. Note that the NMR signal voltage from a hyperpolarized sample scales linearly with B_0 [41], nonetheless, sufficient SNR for high-resolution MRI can be achieved at B_0 ~ 10 – 100 mT due to reduced sample (tissue) noise, and increased T_2 and T_2^* because of the reduced effect of susceptibility-induced background field gradients. Thus, as we have shown previously [39,40,42,43,31], hyperpolarized ^{3}He MRI can be performed at B_0 substantially lower than in clinical scanners, ~ 10 mT (100 G), with SNR and resolution for lung imaging approaching that obtained in clinical scanners. This fact enables us to exploit dramatic simplifications in magnet technology in the very-low-field regime (~ 10 mT), such as open-access electromagnets, that enable a walk-in, open scanner where a subject can sit, stand, lie horizontal or recline at any angle [42,31].

We first demonstrated hyperpolarized gas MRI at very-low-field with glass ^{3}He cells and inflated rat lungs in a 30 cm-bore solenoidal resistive magnet operating at ~ 2 mT (20 G)

[39,40]. This system achieved ~ 4 mm image resolution and benefited from the reduction of susceptibility-induced gradients in rat lungs, where a ^{3}He T_2^* of ~ 100 ms was measured, which compared favorably to that measured at 1.5 T (~ 5 ms) [39]. More recently, several groups have performed in vivo human lung ^{3}He MRI at fields of 0.15 T [44], 0.1 T [45], 15 mT [46], and 3 mT [47,48] using clinical scanners with resistive [45,48], permanent [44] or ramped-down superconducting [46] magnets. One study has been performed with a subject standing in a resistive magnet system operating at 3 mT [47]. As a first step to hyperpolarized ^{3}He orientation-dependant imaging, we assembled a prototype, open-access human imaging system and acquired preliminary human lung images in two postures (vertical and supine) at B_0 ~ 4 mT [42,43].

The open-access imager described here has greatly improved performance, in particular B_0 homogeneity, gradient performance, noise filtering, and gradient coil heat dissipation. This system will enable quantitative, high-resolution maps of lung ventilation and function with the subject in different body orientations and provide pulmonary physiology with a powerful tool for studying posture-related effects. In this manuscript, we describe the components of this system in detail, including several novel sub-system designs. We show NMR and MRI performance characteristics for the system and initial ^{3}He human lung images. We also discuss unique challenges and advantages associated with imaging at unconventionally low frequencies (200–300 kHz) with our apparatus and assess the potential of this imager as a powerful tool in the investigation of pulmonary dynamics and pathophysiology.

2 System Overview

A simplified schematic of the open-access imager (OAI) is shown in Figure 1. Figure 2 shows the fully assembled OAI electromagnet and gradient coils, as well as the open-access imaging region and the defined imaging axes. The lower operating frequency and the smaller B_0 places a different set of physical and technical requirements and constraints for the individual components of the OAI compared to a conventional high-field system. In the following sections we detail the designs and specifications of these components and highlight some of the more novel aspects of the OAI.

2.1 Open-Access B_0 Electromagnet

The open-access electromagnet design goals were an inter-coil separation of ~ 90 cm allowing walk-in access, an imaging region of 40 cm diameter spherical volume to cover the lungs, a 100 ppm B_0 homogeneity, and the capability to generate up to a 10 mT B_0 field. To achieve these goals while maintaining a small physical footprint, we employed a four-coil, bi-planar, 8th order magnet design. A theoretical study by Morgan et. al. found that such designs can have a large inter-coil separation and produce a homogeneous magnetic field over a large region, making them well-suited for multi-orientation imaging of humans [49]. We believe this is the first experimental realization of such a coil design for human MRI. Figure 3 shows a theoretical plot of B_0 homogeneity obtained using Biot Savart software [Ripplon Software, Inc]. One particular advantage to this arrangement is its relative insensitivity to positional misalignments. More typical four-coil geometries based on the distribution of currents on a sphere (e.g., ”tetracoil” [50]) produce a superior B_0 homogenity with a comparable footprint, however a z-axis misalignment of 1 mm of a single coil in this arrangement reduces the B_0 homogeneity over a 40 cm DSV by over an order of magnitude. In contrast, our bi-planar arrangement suffers only a two-fold decrease in overall homogeneity across the same region for the same misalignment.

The outer B_0 coils measure 2.10 m in diameter from the center of the wiring on one side to the other. Each coil contains 163 turns of square 6-AWG polyester-insulated copper wire [MWS Wire Industries, Inc], wound in a 12 × 14-layer configuration, with seven windings across the

final top layer. The position of this last layer was also numerically calculated to optimize B_0 homogeneity. We used a high-viscosity thermally-conductive epoxy [832TC, MG Chemicals] to bind the wiring tightly onto two circularly-bent aluminum L-channels that are pre-mounted on a large 2.21-m circular aluminum flange whose circumference deviation was less than 2 mm from the mean value. We wound the coils with the flanges in a horizontal position, and then lifted the flange into a vertical orientation for mounting to its frame. Each coil and flange set has a combined mass of ~ 340 kg. The DC resistance for each coil is 1.1 Ω at 25° C.

The inner coils are co-planar with the outer ones. Each carries four windings using the same square copper wiring as the outer coils, and are bound with the same thermal epoxy to a Nylatron™ circular disk. The disks are attached to the main aluminum flanges that hold the outer coils, via spring-loaded screws which allow up to 10 mm adjustments to be made along the *z* axis for B_0 optimization. The DC resistance for each inner coil is < 0.01 Ω at 25° C. Each flange and coil set is separated by ~ 90 cm. The flanges themselves are mounted vertically on a customized frame made from 90 mm × 90 mm extruded aluminum beams with mounting channels [Bosch-Rexroth]. The frame design allows high-precision translational (±1 mm) and rotational (±1 mRad) alignment of the flanges before locking the coils into position, and maintaining the desired inter-coil separation to within 1 mm.

All four B_0 coils are connected in series to a single DC power supply [Alpha Power, Inc] capable of providing up to 45 A with a stability better than 15 ppm after modification to incorporate an Ultrastab 867 direct current-current transformer [Danfysik, Denmark] as the input to the current feedback loop. The B_0 coils output a magnetic field strength of 1.54 G/A, giving a maximum possible B_0 of ~ 7 mT. The power supply is constantly cooled by a recirculating water chiller [CFT-33, Neslabs, Inc.]. With a more powerful current supply, we expect the B_0 system will be able to provide up to 10 mT with good homogeneity.

We typically operate the OAI with B_0 = 6.5 mT (65 Gauss), which is obtained with a current of 42.2 A, and allows ^{3}He NMR/MRI at 210 kHz. Under these conditions the total resistive heat dissipation—which is essentially all from the outer B_0 coils—is approximately 6000–7000 W. We use both active and passive techniques to cool the coils during operation. The outer B_0 coils are wound against an aluminum L-channel as part of the mounting flange; thus two sides of the copper wiring are exposed to air and two are in contact with the flange. We applied a silver-based thermally-conductive paste between the L-channel and the flange, allowing the flange to act as a large heat sink for the outer B_0 coils. The bulk of the heat removal, therefore, is performed by convective air flow. Additionally, we use a 2000 W recirculating liquid chiller [CFT-175, Neslabs Inc.] and pump a mixture of ethylene glycol and water through two 0.5-inch copper tubes in a counter-current fashion. The coolant is run at 15° C and is continuously pumped while the OAI is on. When the B_0 current is at 45 A, the equilibrium coil surface temperature is < 70° C, while the flange temperature near the cooling tubes never exceeds 40° C.

Optimization of B_0 homogeneity was performed by minute adjustments to the B_0 coil/flange positions on their aluminum frame, and by adjustments to the Nylatron frames of the inner coils. After each adjustment, a B_0 field map was made from NMR measurements performed with ”Coil A”, and a 50 cm^3 water sample. Once the flanges were locked down, further B_0 homogeneity improvements were made by adding passive ferromagnetic shims (6 × 6 inch^2 0.006 inch-thick steel sheets) to the back of the aluminum flanges, just behind the outer B_0 coils. A new B_0 field map was acquired with each new arrangement and used to guide the following adjustments. As the homogeneity improved we left each new shim arrangement with the B_0 on for at least a half hour to allow the steel sheets to thermalize and their magnetization to settle. After several iterations, we achieved an eight-shim arrangement with good B_0 homogeneity across a 25 cm diameter region at the center of the magnet: $\Delta B_0 \sim \pm 0.02$ G or

about 350 ppm. An example ^{1}H frequency map of B_0 following optimization is shown in Figure 4.

2.2 Open-Access Gradient Coils

To maintain the open-access environment we designed and constructed a set of planar magnetic field gradient coils for each of the three cartesian axes, which can be seen in Figure 2. This differs from conventional cylindrical gradient coil forms, which offer better efficiency (magnetic field output per unit of current) at the expense of physical access. Our gradient designs were subject to the following constraints: (i) production of B_z magnetic field gradients with strength and linearity suitable for 0.5 mm image resolution over a 40 cm DSV; (ii) inductive- and impedance-matching to current amplifiers originally designed for a conventional MRI system; (iii) size not exceeding the mounting space on the aluminum flanges and the inter-coil separation of the B_0 coils; and (iv) separation of the *x* and *y* gradient pairs by about 1 cm to enable mounting and heat dissipation. For ^{3}He (γ = 3.24 kHz/G), the above constraints implied a minimum readout gradient field strength of 0.077 G/cm; deviation from linearity of less than 0.006 G; and slew rates that allowed current ramp-up times of ~ 500 μs.

We designed bi-planar gradient sets to produce linear *x*, *y*, and *z* magnetic field gradients, according to the above constraints, using an in-house field-mapping and optimization program written in MATLAB [Mathworks, Inc].

We also added translation tools to export these paths to the CAD program Vectorworks [Nementschk Inc.] for coil mount designs. The MATLAB program iteratively adjusts coil design parameters while calculating B_z and minimizing the deviation from a perfect linear gradient. After a coil optimization routine was complete, the software produced B_z field maps across several slices of the 40 cm DSV region and a calculation of the magnetic field gradient strength in G/cm, as shown in Figure 5. We provided to the software an initial input current of 180 A, near the 200 A maximum current capability of the gradient amplifiers, as well as an initial wiring pattern for each gradient coil.

The *z* gradients were based on a Maxwell pair configuration with additional correction loops to expand the region of gradient linearity to cover the region of interest. The final *z* gradient coil design consists of five loops total for each plane, with an inter-planar separation of 88.0 cm. The loops are arranged in three sections: an inner loop of radius 5.0 cm, a middle loop with radius 43.8 cm, and three outer loops wound together with radii 71.0 cm, 71.5 cm, and 72.0 cm, as seen in Figure 6. The coils were wound around aluminum forms using insulated round 5 AWG solid copper wire [MWS Wire Industries] and set using the same thermal epoxy used for the B_0 coils. The photograph in Figure 2 shows the coil framework. Connections between the coil loops are made in series while the entire planar coil is wired in series to its opposite pair. The DC resistance of the entire *z* bi-planar gradient set is 0.08 Ω, with an inductance of ~160 μH.

The design for the transverse (*x*, *y*) gradient coils was based on a planar projection from a cylindrical Golay coil. We used rectangular loops to simplify the calculations and coil construction methods, and as with the *z* gradients, added more loops to include higher-order corrections to enhance gradient field linearity. We then used the optimization software to determine the ideal loop separations. Figure 6 shows one such coil arrangement. The *x* gradient coil planes are separated by 81 cm. The optimal number of loops for each planar coil was 5 for each half (10 total). Coil loop dimensions are given in the figure caption. The width and height of the entire plane are both 1.4 m. Each coil is wound about a custom-built Nylatron frame slotted to accomodate the *x* gradient coil plane on one side and a *y* gradient coil plane on the other (separated by 1.0 cm). The coil wire and epoxy are the same materials used for the *z* gradient coils. The *y* gradient coil planes are almost identical in form to the *x* coils, except they

are oriented orthogonally, separated by 79 cm, and possess slightly different coil loop distances. Both transverse gradient coils possess similar circuit characteristics: the total DC resistance for each bi-planar pair is 0.09 Ω and the inductance is ~ 90 μH.

All three planar gradient sets are mounted using machined aluminum bars and L-channels to the same aluminum flanges that support the B_0 coils. The mounts include slotted brackets that allow 4 cm of translational and 4° of rotational adjustment for each plane. The *z* gradient coils are mounted independently of the transverse gradients, so the two sets can be adjusted separately. The *y* gradients are flush with the L-channel support of the outer B_0 coils, the resulting 79-cm gap represents the maximum spacing available for the imaging subject. We minimized the potential for eddy current effects by assembling the *z* gradient frame using plastic and teflon spacers, which prevented electrical contact between the aluminum components. The transverse gradient frames were fashioned entirely out of (electrically-insulating) Nylatron and assembled using nylon screws. Additionally, we cut 50 μm slots in a sunburst pattern in the aluminum flanges from the center to the outer B_0 coils to inhibit the flow of any remnant eddy currents.

Each planar gradient set is powered by a Techron 8607 Series gradient amplifier. The gradient coils were designed to have a very low DC resistance to avoid excessive heating; however the gradient amplifiers require a minimum load of 0.5 Ω for proper circuit stability and to protect the amplifiers from driving excessive currents. We therefore built a resistor bank to increase the total circuit gradient loop resistance to 0.5 Ω. The bank consists of three separate rows of 300 W, 5 Ω wire-wound power resistors [MultiComp]. Each row consists of 12 of these resistors wired in parallel, yielding a net resistance of 0.41 Ω During a typical gradient echo imaging sequence, the peak resistive dissipation can reach as high as 6–8 kW per channel over the course of 10–20 seconds, which occurs largely in the resistor bank located safely outside of the OAI Faraday cage and away from the imaging area. As the gradient amplifiers themselves are typically matched to a 1 mH inductive load, we reconfigured the compensation circuit on the front board of the Techron amplifiers to achieve inductive matching for this circuit. When driving the gradient coils and resistor bank, each Techron amplifier provided ~ 140 A peak current, which yielded a maximum gradient strength on each axis of approximately 0.07 G/cm (i.e., 5×10^{-4} G·cm^{-1}·A^{-1}). The measured deviation in gradient linearity was less than 1% for all axes.

2.3 RF Coils and Electronics

We built several solenoidal RF coils for different tasks on the OAI, including B_0 mapping, gradient field calibration, phantom NMR studies, and human lung imaging. Table 1 shows specifications for three of the most frequently used coils on our system. These coils operated at ~ 210 kHz for ^{3}He or ~ 275 kHz for ^{1}H, corresponding to B_0 = 6.5 mT. The tuning and matching capacitors, C_T and C_M, for each coil were housed inside a circuit box that was connected by standard coaxial cables, and was distant from the coil itself. We typically added resistors in series with C_M to both raise the coil impedance to 50 Ω and lower the coil *Q* factor, which was required for proper bandwidth matching at our unconventionally low operating frequencies. For example, the response function of a coil with a *Q* of ~ 20 (at 210 kHz) is comparable to the 5–10 kHz frequency-encode bandwidth typically used for our imaging experiments.

In particular, for human lung imaging we built a chest coil large enough to cover the thoracic region and allowing the subject's arms to be kept within the coil. The coil form is made of compressed cardboard cut to a length that reaches from the top of the subject's hips to the bottom of his or her chin, so that the subject can be imaged in a sitting or standing position and still have access to a ^{3}He delivery tube. The coil wire is fixed to the cardboard tube with a fast-acting clear epoxy and wrapped beneath a rubber insulating sheet for safety purposes.

To characterize the B_1 profile of the human chest coil, we performed hyperpolarized ^{3}He flip-angle calibration measurements, using a method described previously [40]. As shown in Figure 7, the ^{3}He flip-angle, and hence the B_1 profile, is well-described by the functional form for the magnetic field created by an ideal solenoid of finite length L and radius R along its central axis at position x [51]:

$$B(x) \propto \left[\frac{x}{(R^2+x^2)^{\frac{1}{2}}} + \frac{L-x}{(R^2+(L-x)^2)^{\frac{1}{2}}} \right]. \quad (1)$$

As expected, we found a variation of ~ 5% in the flip-angle along the central 30 cm of the coil.

To test sample loading of the human chest coil, we used a Bravo MRI impedance analyzer [AEA Technology Inc] to obtain standing wave ratio (SWR) plots with the chest coil unloaded and with different human subjects. As shown in Figure 8, we found that the resonant frequency shifts downwards but the coil Q is unaffected, as expected for low RF frequencies where sample (tissue) noise and loss is generally small [41,43,52]. For imaging subjects weighing between 60–80 kg, the resonant frequency shift is about −2 kHz. We therefore shifted the unloaded coil resonance by +2 kHz so that the coil resonance would be centered at ~ 210 kHz when a typical human subject is present.

The OAI spectrometer consists of an Apollo MR research console [Tecmag, Inc.] for RF and gradient pulse control and low-frequency signal reception. The Apollo includes a 2 kHz to 100 MHz RF transmitter, allowing MRI at 210 kHz without additional mixing hardware. The system includes an external gradient controller with three DSP waveform generators which perform digital pre-emphasis on the fly, and provide offsets for x, y and z shimming. The transmitter output of the Apollo is connected to a NMR Plus 5LF300S amplifier [Communications Power Corp], which delivers 300 W of RF power across the range of 100 kHz to 1 MHz, and includes blanking circuitry driven by the spectrometer. The amplifier connects directly with a Transcoupler II probe interface [Tecmag] with a 1/4-wave lump element optimized for 200 kHz operation, allowing RF coils to function both for RF transmission and signal detection. The NMR signal is amplified by an AU-1583-9421 pre-amplifier [Miteq, Inc.], which provides ~ 36 dB gain above 200 kHz, before reaching the Apollo receiver.

There can be significant environmental noise within the 200–300 kHz frequency range. Thus the OAI magnet, gradient coils, and RF coil are housed inside a 4 feet wide × 8 feet long × 7.5 feet tall Faraday cage [82 Series, Lindgren Inc.] designed to attenuate RF interference in the range of 10 kHz to 10 MHz by up to 100 dB. The upper half is constructed using copper mesh, allowing air flow for convective B_0 cooling. All electrical connections from outside are passed into the room using passive filtering boxes that shield out noise above 10 kHz [Lindgren Inc]. These include a 110V, 60 Hz power supply for electronics inside the room and power lines for the B_0 coils and the preamplifier. The three gradient power lines are introduced into the Faraday cage via three sets of custom high-current feed-through passive line filters that produce ~ 25 dB attenuation at ~ 100 kHz [Schaffner, Inc].

3 Demonstration Imaging: Methods

We typically hyperpolarized ^{3}He cells to 10–15% by performing spin exchange optical pumping (SEOP) for 6–20 hours. Details of the SEOP polarizer and ^{3}He production can be found elsewhere [42]. For 2D MRI we used gradient-recalled echo (GRE) sequences with flip angle θ ~ 2–5°., 128 frequency × 64–128 phase encodes, T_R ~ 60–100 ms, T_E ~ 30 ms. We tested all ^{3}He imaging sequences with the human chest RF coil oriented in both x (“supine”)

and *y* ("upright") positions. 3D sequences were identical to 2D sequences with the exception of a second phase encode gradient with 6–8 slices and the use of centric phase encoding schemes. We tailored the 3D scans to be performed in under 30 seconds to allow comfortable imaging under a single breath hold. The readout gradients were always applied along the *z* axis. For human imaging, this has the advantage that the same gradient can be used as the read gradient for both supine and upright imaging, allowing us to compare images more reliably.

We used simple wooden furniture to enable supine or upright imaging of our human subjects (Figure 9), with adjustable independent support for the RF coil to minimize transmission of motion from the subject to the coil. In both orientations, the RF coil can be slid away or raised above the subject, allowing the subject to be positioned with ease. For human experiments, subjects took three or four deep breaths of air prior to ^{3}He inhalation. The hyperpolarized ^{3}He was delivered from the polarizer to a Tedlar plastic bag. (^{3}He $T_1 > 20$ minutes inside the bag.) After filling, the bag was sealed off from the polarizer. Once the subject was at relaxed expiration, a pneumatically-operated valve allowed the subject to inhale 400–500 cm^3 of hyperpolarized ^{3}He via an inhalation tube. To facilitate the breath hold during imaging, the subject then inhaled an additional 100–150 cm^3 of room air and held their breath for 30–40 s while MR images were acquired. The subject's blood pressure, heart rate and S_pO_2 levels were monitored before and after the experiment, in compliance with IRB requirements. All human ^{3}He inhalation experiments were performed according to protocols approved by the Partners Human Research Committee of the Brigham and Women's Hospital, under an inter-institutional IRB agreement with Harvard University.

4 Demonstration imaging: Results

We used the OAI to demonstrate human lung ^{3}He MRI with a volunteer subject in both the supine and upright sitting positions. In various runs without imaging gradients, we measured $T_2^* = 15 - 17$ ms for ^{3}He inhaled into the lungs, which is consistent with the expected value given the measured B_0 homogeneity over the lung volume (see Figure 4). Figure 10 shows example human 2D projection and 3D MR lung images. The 2D projection images show well-defined pleural boundaries with $SNR_{pixel} > 50$. The cardiac profile can be seen in the medial aspect of both right and left lungs, and both lateral and antero-posterior diaphragm curvature is evident. The image intensity is greatest nearer the middle-to-inferior and lateral aspects of the lung, where the anterio-posterior dimensions of the lung are thickest. The 3D image clearly shows the region where the heart resides, with a larger cavity on the medial aspect of the left lung than on the right, as expected. There is even distribution of ^{3}He ventilation throughout the periphery of the lung; and the regions exhibiting the greatest antero-posterior thickness correspond to the greatest signal intensity in the 2D projection images. There is also a faint ^{3}He signal in the left bronchus but not in the right, which we attribute to residual ^{3}He remaining in the large airways after the subject's chaser breath of room air. This result is consistent with anatomy: the left bronchus has a slightly sharper branching angle, and thus gas flow through the region is lower in comparision to the right bronchus.

5 Discussion

The initial human ^{3}He lung images obtained with the OAI provide clear definition of different regions of the lung, exhibit good SNR and are artifact-free, for both supine and upright body orientations. These results are a significant improvement over images obtained previously at 3.9 mT using our prototype open-access imager [43,42], and by others at $B_0 < 0.1$ T [46,48]. In future work, we plan to implement slice selection, which will improve the visual quality of 2D anatomical images. We note, however, that slice selection must be employed carefully in quantitative functional studies such as pulmonary oxygen partial pressure and Apparent

Diffusion Coefficient (ADC) mapping, due to the rapid diffusion of polarized ^{3}He spins into the slice of interest [53,54].

5.1 Image SNR

The nuclear spin polarization of hyperpolarized noble gas is B_0-independent. In addition, at very low magnetic fields, electronic Johnson noise of the coil [55], dominates over sample noise. Therefore, the expected SNR for very-low-field NMR of hyperpolarized ^{3}He is:

$$\mathrm{SNR}=\frac{(B_r/i_r)V_s\rho P\gamma^2 B_0}{2\sqrt{4RkT\Delta f}}. \tag{2}$$

Here (B_r/i_r) is the magnetic field strength (per unit current) of the pickup coil, V_S is the sample volume, ρ is the spin density, P is the ^{3}He spin polarization and γ is the gyromagnetic ratio for ^{3}He; R is the coil resistance, k is the Boltzmann constant, T is the pickup coil temperature and Δf is the receiver bandwidth (inversely proportional to T_2^*). Assuming P = 0.15, 500 cm^3 of ^{3}He diluted into a 6 L total gas volume to represent a lung sample, and taking the calculated value $B_r/i_r \simeq 6.5\times10^{-5}$ T·A^{-1} for our solenoidal chest RF coil at room temperature, Equation 2 yields an expected SNR ≃ 240,000 for a typical ^{3}He T_2^* ~ 15 ms in the OAI. The pixel SNR can then be calculated using the relationship [56]:

$$\mathrm{SNR}_{\mathrm{pixel}}=\frac{4}{\pi}\frac{N}{N_0^2}(\mathrm{SNR})\,e^{-\frac{t_{\mathrm{acq}}}{T_2^*}}\sin\theta, \tag{3}$$

where N is the number of pixels in an $N \times N$ image, N_0 is the number of pixels encompassing the object, SNR is given by Equation 2, t_{acq} is the echo acquisition time and θ is the flip angle. For a 2 cm slice, N = 256, N_0 = 150 (assuming 2 mm pixels across a 30 × 30 cm lung), matched filter condition $(t_{\mathrm{acq}}/T_2^*=\pi/2)$, and a flip angle of 10°, we find an expected $\mathrm{SNR}_{\mathrm{pixel}}$ ~ 50.

This estimate agrees well with our observed values of $\mathrm{SNR}_{\mathrm{pixel}}$ from the images in Figure 10. The 2D images without slice selection have $\mathrm{SNR}_{\mathrm{pixel}}$ ~ 25–80 (supine) and 50–140 (vertical), while the 1.5 cm image planes from the 3D dataset have $\mathrm{SNR}_{\mathrm{pixel}}$ ~ 40–60 (central slices) or 15–30 (peripheral slices). These images were acquired with the following parameters: N = 128, N_0 = 75, θ = 4°. Equation 3 can therefore be used to calculate the maximum sample SNR that would have been observed from a single 90° RF pulse in these experiments. For the 2D projection images, maximum theoretical sample SNR ~ 100,000–150,000, while for the 3D dataset, which was acquired after optical pumping of ^{3}He with a novel, wavelength-narrowed laser source, SNR ~ 280,000. These results clearly demonstrate that SNR suitable for pulmonary functional imaging, i.e., $\mathrm{SNR}_{\mathrm{pixel}}$ ~ 50, is currently obtainable using the OAI with our helium polarization apparatus. Improvements currently being performed to our helium polarizer to increase production rate and yield of hyperpolarized ^{3}He will only increase the attainable SNR. [Note: the maximum theoretical SNR calculated above was not observed in practice, as low-flip angle excitations are used to preserve the hyperpolarized ^{3}He magnetization.]

5.2 ^{3}He T_2^* in human lungs at 6.5 mT

There are several major contributors to T_2^* for ^{3}He in the lung:

$$\frac{1}{T_2^*}=\frac{1}{T_2}+\frac{1}{T_{2,\text{in}}}+\frac{1}{T_{2,\text{sus}}}+\frac{1}{T_{2,\text{diff}}}+\frac{1}{T_{2,\text{grad}}}, \tag{4}$$

where T_2 is the intrinsic decoherence rate, set primarily by T_1 relaxation due to motion of ^{3}He atoms past paramagnetic O_2 molecules ($T_2 \simeq T_1 \simeq 10$ s for typical pulmonary O_2 concentration [57]); $T_{2,\text{in}}$ is the contribution from B_0 inhomogeneity, $T_{2,\text{sus}}$ arises from magnetic susceptibility-induced gradients in the local magnetic field; $T_{2,\text{diff}}$ describes decoherence due to ^{3}He diffusion through local field gradients; and $T_{2,\text{grad}}$ accounts for decoherence due to diffusion through applied imaging field gradients. Equation 4 can be re-written with explicit expressions for each T_2^* contribution:

$$\frac{1}{T_2^*}=\Gamma[\,O_2]+\frac{\gamma\Delta B_0}{2}+\frac{\gamma\Delta\chi B_0}{2}+(\gamma\Delta\chi B_0)^2\frac{l^2}{D}+\frac{\gamma^2G^2TE^2D}{12}, \tag{5}$$

where $[O_2]$ is the pulmonary O_2 concentration and Γ is the associated rate constant for ^{3}He T_1 relaxation ($\simeq$ 2.61 bar·s^{-1} [58]); γ is the gyromagnetic ratio; $\Delta B_0 \simeq 0.04$ G is the B_0 inhomogeneity in the OAI across a typical lung; $\Delta\chi \simeq 9\times10^{-6}$ [59] is the magnetic susceptibility difference between tissue and gas, $l \simeq 20$ μm is the characteristic gas diffusion length in the lung before hitting a boundary; $D \simeq 0.15$ cm^2·s^{-1} is the ^{3}He restricted diffusion coefficient inside the lung and mixed with 37° C air; G is the imaging gradient (≃0.05 G·cm^{-1} in the OAI and 1 G·cm^{-1} in a clinical scanner); and TE is the echo time of the imaging experiment (≃30 ms in the OAI, 4 ms in a clinical scanner).

Table 2 summarizes the typical ^{3}He T_2^* contributions for the entire lung at 1.5 T using clinical MRI scanners and at 6.5 mT using the OAI. Note the greatly reduced influence of $T_{2,\text{sus}}$ and $T_{2,\text{diff}}$ at low B_0. Effects from $T_{2,\text{grad}}$ are similar at both fields because the longer echo time required at low fields offset by weaker imaging gradients in the OAI in comparison to values used in a clinical scanner. With further upgrades, we expect to improve the OAI B_0 homogeneity by a factor of ~ 3–4, which should enable ^{3}He $T_2^* > 40$ ms.

5.3 Limit to ^{3}He Lung Image Resolution using the OAI

The limit to lung image spatial resolution, Δx, using the OAI and assuming sufficient ^{3}He SNR during a single breath-hold, is dependent on both T_2^* and the diffusive properties of ^{3}He, as described by [56,40,41]:

$$\Delta x=1.34\left[\Delta x_{\text{diff}}(\Delta x_{T_2^*})^2\right]^{\frac{1}{3}}. \tag{6}$$

Here, $\Delta x_{T_2^*}$ is the T_2^*-based resolution limit, and Δx_{diff} is the ^{3}He diffusion-based resolution limit.

T_2^*, and by implication the spectral linewidth, sets fundamental limits on resolution for any MRI system. To achieve a spatial resolution of N pixels across a sample, the imaging system must operate at a bandwidth of $N \times$ FWHM, where $\text{FWHM}=\frac{1}{\pi T_2^*}$. This places a limit based on the magnetic field gradient strength G [56]:

$$\Delta x_{T_2^*} = \frac{2}{\gamma G T_2^*}. \quad (7)$$

For G ~ 0.1 G/cm and T_2^* ~ 15 ms, both typical values for ^{3}He on the OAI, $\Delta x_{T_2^*} \sim 4.1\text{mm}$. The diffusive properties of ^{3}He gas provide a similar limitation to the available imaging resolution. Δx_{diff} is set by the characteristic diffusion length traveled by the ^{3}He nuclei during the sampling acquisition time t_{acq}:

$$\Delta x_{\text{diff}} = \sqrt{2 D t_{\text{acq}}}. \quad (8)$$

Given $t_{\text{acq}} = \pi T_2^* \sim 47\text{ms}$ (matched filter conditions) and $D = 0.15\ \text{cm}^2 \cdot \text{s}^{-1}$ for ^{3}He gas in residual air in human lungs: Δx_{diff} ~ 1.2 mm. Combining the results for Δx_{diff} and $\Delta x_{T_2^*}$ into Equation 6, the overall resolution limit for the open-access imager under typical conditions is Δx ~ 3.6 mm, close to the value of 3.9 mm actually obtained in our lung images. A doubling of the *z* gradient strength to *G* ~ 0.2 G/cm, as discussed below, would reduce $\Delta x_{T_2^*}$ ~ 2.1 mm and the corresponding value of Δx ~ 2.3 mm, similar to the resolution of ^{3}He MRI images obtained at 1.5 T (2 × 2 × 20 mm) [7,8,10].

Obtaining useful images at image-resolution limits is only possible if sufficient SNR is available for such image resolution. Using Equation 3, and a flip-angle, θ = 4°, we can calculate that to achieve an image with a minimum $\text{SNR}_{\text{pixel}}$ ~ 5, the minimum total SNR from the sample must be ~ 6000 for a 2D projection image and ~ 35,000 for a 3D image at the currently obtainable image-resolution limit of 3.6 mm. As discussed earlier in this section, such SNR values are routinely exceeded, and $\text{SNR}_{\text{pixel}}$ at a resolution of 3.9 mm has greatly exceeded a limiting value of 5, generally by at least an order of magnitude. To achieve an image resolution limit of 2.3 mm, maximum SNR will need to be higher than in the 3.6 mm-resolution case. For a 2D projection image with a resolution ~ 2.3 mm, a maximum sample SNR ~ 12,000 is required, while for a 3D image with 2 cm slice thickness, SNR of ~ 70,000 will be necessary. Again, such values of SNR are achievable with our current polarizer hardware, and therefore we can expect images with sufficient SNR at a limiting-resolution of 2.3 mm once gradient hardware is modified to allow this resolution to be achieved.

5.4 Hardware Performance

The design of the OAI system was guided by an understanding of opportunities and limitations encountered in the operation of the prototype open-access imager described previously [43]. These centered around a few key areas: (i) RF coil design, minimal loading by human subjects at low field, and the use of high-*Q* coils at low frequencies; (ii) gradient strength and resulting concomi-tant field effects; and (iii) noise filtering, especially on gradient lines. Below, we briefly describe our approach in these areas.

We implemented a single transmit-receive chest coil for human MRI, in order to avoid coil alignment and cross-talk problems experienced previously. Additionally, given the orientation of B_0 in the OAI, we chose to use a solenoid coil design. As shown in Figure 7 and Figure 8, the solenoid coil exhibits a highly uniform B_1 field in which coil loading by human subjects is negligible. Hence we can easily calibrate the excitation RF flip angles beforehand, rather than having to include such calibrations as part of every quantitative MRI sequence. In-tegrated flip-angle calibration is essential in high-field scanners for functional lung imaging techniques such as oxygen-mapping, where the excitation flip angle must be known precisely [9,10], which

make this method time-consuming and complex in such scanners. Our combination of low-frequency operation and a highly-uniform solenoidal coil form will drastically simplify such measurements in the OAI.

A second unusual feature of performing MRI at very-low-field relates to the frequency bandwidth of the coil, and how for tuned coils with high Q, this approaches the imaging bandwidth of an MRI experiment [43]. At high frequencies, resonant high-Q coils are used to maximize NMR signal sensitivity in a condition where the frequency bandwidth of the coil is always much greater than the imaging bandwidth: e.g.; at a Larmor frequency of 63 MHz, a tuned coil with a $Q \sim 100$ results in a coil response function with full-width half-maximum ~ 630 kHz. In the OAI, by contrast, high-Q coils are problematic; at a Larmor frequency of 200 kHz, a tuned receive coil with a Q of greater than ~ 20 results in a coil response function that significantly attenuates a typical frequency encoding bandwidth of 20 kHz. The use of a high-Q receive coil in this instance would result in the frequency-encoded signal outside of the narrow coil response function being attenuated significantly [43,47], possibly to the extent of being unrecoverable via post processing. Thus, we have employed low-Q coils with a high filling factor design to mitigate the issue of finite coil bandwidth at low frequencies [60–62]. Lowering the coil Q results in a slight, but inevitable trade-off in image SNR [60,62], however the large signal obtained from hyperpolarized samples allows this to be tolerated to some degree. As a result, we have obtained images (Figure 10) with high SNR that do not suffer variable attenuation across the image frequency range due to a convolution of the coil response on the image data, nor non-uniform noise floors (as were observed previously and which required considerable post-processing in order to partly correct the effect [43]).

We also intentionally employed low gradient strengths in the OAI to avoid concomitant field effects from the gradient field approaching the value of B_0. For the current operating conditions ($B_0 \sim 7$ mT, $\delta B \sim 1$ mT/m or 0.4 mT/40 cm FOV), we estimate that there is radial distortion of an image due to concomitant field effects with a radius of curvature of 8 m for the maximum values of our encoding gradients [63]: ~ 20 times the acquired FOV for lung imaging. Correspondingly, our lung images (Figure 10) are free of any radial distortion. We note that the gradient strength in the OAI could still be doubled by adding a second gradient amplifier in series to the first, thereby increasing imaging speed without any significant imaging artifacts due to concomitant field effects.

As discussed in Section 2.3 above, isolation of the OAI from environmental noise in the range ~ 100–300 kHz was realized by housing the magnet system in a Faraday cage, and using filters on the B_0 power supply lines and RF and electrical power connections. Filtering out noise on the gradient lines while passing common gradient slew frequencies (~ 1–2 kHz) was especially challenging for MRI at these frequencies, since the Techron gradient amplifiers output excessive noise in the 100–300 kHz range, and commercial MRI gradient filters do not block noise at this frequency range. However the custom Schaffner filters we employed in the OAI provided more than an order of magnitude attenuation of gradient line noise relative to the previous prototype low-field imager [43].

While the discussion in Section 5.2 above highlights the benefits of operating at $B_0 \sim 0.1$ T, we note that a slight increase in B_0 (~ 2–5) would significantly ease constraints on the areas of imager design discussed above. Higher-Q RF coils could be used to increase detection sensitivity further, while narrow coil bandwidth issues would be reduced. Higher gradient strengths could be used without concern for concomitant gradient effects, and in combination with wider bandwidths would allow a greater exploitation of the very long T_2^* values observed in this B_0 regime. These additional improvements could be achieved while still operating below the "body-noise dominance" region, and so maintaining the benefits of consistent B_1 calibration without coil-loading effects, and minimal T_2^* losses due to susceptibility effects. As stated in

Section 2.1, the magnet was designed to operate at almost twice the B_0 currently used for our imaging experiments, and this higher B_0 will be achieved with a future upgrade to the magnet power supply.

Finally, we note that as the main magnetic field and operating RF frequencies of the OAI are extremely low in comparison to typical clinical MRI scanners, the OAI is operated well within the FDA approved limits for deposited RF power (SAR), gradient slew rate ($\delta B/\delta t$), and acoustic noise. SAR scales with B_0^2, hence for the OAI, SAR for a typical FLASH imaging experiment are ~ 40,000 times below those experienced in a clinical imager, and 10^7 times below FDA limits. $\delta B/\delta t$ does not exceed 5 T/s on the OAI when reaching the maximum gradient strength – a value for $\delta B/\delta t$ that is 4 times lower than the FDA limit. Additionally, the gradient coils in the OAI operate at their maximum currents and slew rates without the generation of any audible acoustic noise, owing to very low Lorentz forces at our very low B_0 strength.

6 Conclusions

We have developed and begun operation of an open-access, very-low-field MRI system for *in-vivo* hyperpolarized ^{3}He human lung imaging as a function of subject posture. The imager is based on a bi-planar B_0 coil design that has been optimized to operate at 65 G (6.5 mT), enabling ^{3}He NMR and MRI at 210 kHz. The imager includes three-axis bi-planar gradient coils that leave a 79 cm inter-coil gap for subject access. The direction of the B_0 field allows the use of a single solenoidal RF coil for subjects in all postures, providing an invariant B_1 field at all postures. Additionally, at these frequencies, the coil is unperturbed by sample loading effects, enabling accurate pre-calibration of RF excitation flip angles.

We have obtained 2D and 3D ^{3}He images of phantoms with up to 2.8 mm resolution; and 2D and 3D ^{3}He human lung images with subjects either sitting vertically or lying horizontally. The images exhibit high SNR, clear definition of lung regions and the effects of the chest cavity on the lungs, and are artifact-free. The image quality is superior to any previous ^{3}He human lung imaging performed at $B_0 < 0.1$ T. This initial result indicates that the open-access lung imager will provide posture-dependent pulmonary functional imaging with a resolution and sensitivity sufficient for pulmonary physiology research and diagnosis. Initial pulmonary functional studies are currently being performed using the system.

Acknowledgments

The authors acknowledge support from NASA grants NAG9-1166 and NAG9-1489, NSF grant CTS-0310006, NIH grant R21 EB006475-01A1, and Harvard University. We also thank Dr. Mirko Hovrat, Dr. Jim Maddox, Dr. Chih-Hao Li, Ms. Rachel Burke, Ms. Ana Batrachenko, Ms. Rachel Scheidegger and Mr. Dan Chonde for technical assistance with imager, and Dr. Michael Barlow for arranging use of novel lasers for helium gas hyperpolarization. We are indebted to Kenneth Tsai, MD, who acted as observing physician for human imaging trials, and George Topulos, MD, who devised the human protocols.

References

1. Walker TG, Happer W. Spin-exchange optical pumping of noble-gas nuclei. Rev. Mod. Phys 1997;69 (2):629–642.
2. Nacher P-J, Leduc M. Optical-Pumping in ^{3}He with a Laser. J. de Phys 1985;46(12):2057–2073.
3. Leawoods JC, Yablonskiy DA, Saam BT, Gierada DS, Conradi MS. Hyperpolarized He-3 gas production and MR imaging of the lung. Concepts Magn. Reson 2001;13(5):277–293.
4. Moller HE, Chen XJ, Saam B, Hagspiel KD, Johnson GA, Altes TA, de Lange EE, Kauczor HU. MRI of the lungs using hyperpolarized noble gases. Magn. Reson. Med 2002;47(6):1029–1051. [PubMed: 12111949]

5. Salerno M, Altes TA, Brookeman JR, de Lange EE, Mugler JP III. Dynamic spiral MRI of pulmonary gas flow using hyperpolarized ^{3}He: preliminary studies in healthy and diseased lungs. Magn. Reson. Med 2001;46(4):667–677. [PubMed: 11590642]
6. Wild JM, Paley MN, Kasuboski L, Swift A, Fichele S, Woodhouse N, Griffiths PD, van Beek EJ. Dynamic radial projection MRI of inhaled hyperpolarized ^{3}He gas. Magn. Reson. Med 2003;49(6): 991–997. [PubMed: 12768575]
7. Salerno M, de Lange EE, Altes TA, Truwit JD, Brookeman JR, Mugler JP III. Emphysema: hyperpolarized helium-3 diffusion MR imaging of the lungs compared with spirometric indexes–initial experience. Radiology 2002;222(1):252–260. [PubMed: 11756734]
8. Saam BT, Yablonskiy DA, Kodibagkar VD, Leawoods JC, Gierada DS, Cooper JD, Lefrak SS, Conradi MS. MR imaging of diffusion of ^{3}He gas in healthy and diseased lungs. Magn. Reson. Med 2000;44 (2):174–179. [PubMed: 10918314]
9. Deninger AJ, Eberle B, Ebert M, Grossmann T, Hanisch G, Heil W, Kauczor HU, Markstaller K, Otten E, Schreiber W, Surkau R, Weiler N. ^{3}He-MRI-based measurements of intrapulmonary pO_2 and its time course during apnea in healthy volunteers: first results, reproducibility, and technical limitations. NMR Biomed 2000;13(4):194–201. [PubMed: 10867696]
10. Rizi RR, Baumgardner JE, Ishii M, Spector ZZ, Edvinsson JM, Jalali A, Yu J, Itkin M, Lipson DA, Gefter W. Determination of regional V_A/Q by hyperpolarized ^{3}He MRI. Magn. Reson. Med 2004;52 (1):65–72. [PubMed: 15236368]
11. Kauczor HU, Ebert M, Kreitner KF, Nilgens H, Surkau R, Heil W, Hofmann D, Otten EW, Thelen M. Imaging of the lungs using ^{3}He MRI: preliminary clinical experience in 18 patients with and without lung disease. J. Magn. Reson. Imaging 1997;7(1):538–543. [PubMed: 9170039]
12. de Lange EE, Mugler JP III, Brookeman JR, Knight-Scott J, Truwit JD, Teates CD, Daniel TM, Bogorad PL, Cates GD. Lung air spaces: MR imaging evaluation with hyperpolarized ^{3}He gas. Radiology 1999;210(3):851–857. [PubMed: 10207491]
13. Donnelly LF, MacFall JR, McAdams HP, Majure JM, Smith J, Frush DP, Bogorad PL, Charles HC, Ravin CE. Cystic fibrosis: combined hyperpolarized ^{3}He-enhanced and conventional proton MR imaging in the lung–preliminary observations. Radiology 1999;212(3):885–889. [PubMed: 10478261]
14. Altes TA, Powers PL, Knight-Scott J, Rakes G, Platts-Mills TA, de Lange EE, Alford BA, Mugler JP III, Brookeman JR. Hyperpolarized ^{3}He MR lung ventilation imaging in asthmatics: preliminary findings. J. Magn. Reson. Imaging 2001;13(3):378–384. [PubMed: 11241810]
15. Samee S, Altes TA, Powers PL, de Lange EE, Knight-Scott J, Rakes G, Mugler JP III, Ciambotti JM, Alford BA, Brookeman JR, Platts-Mills TA. Imaging the lungs in asthmatic patients by using hyperpolarized helium-3 magnetic resonance: Assessment of response to methacholine and exercise challenge. J. Allergy Clin. Immunol 2003;111(1):1205–1211. [PubMed: 12789218]
16. Remolina C, Khan A, Santiago T, Edelman N. Positional hypoxaemia in unilateral lung disease. N. Engl. J. Med 1981;304:523–525. [PubMed: 6779161]
17. Dean E. Effect of body position on pulmonary function. Phys. Ther 1985;65:613–618. [PubMed: 3991806]
18. Yeaw EM. How position affects oxygenation. Good lung down? Am. J. Nurs 1992;92:26–29. [PubMed: 1536202]
19. Ingimarsson J, Thorsteinsson A, Larsson A, Werner O. Lung and Chest Wall Mechanics in Anesthetized Children: Influence of Body Position. Am. J. Respir. Crit. Care Med 2000;162:412–417. [PubMed: 10934062]
20. Mure M, Lindahl SGE. Prone position improves gas exchange but how? Acta Anaesthesiol. Scand 2001;45:150–159. [PubMed: 11167159]
21. Chatte G, Sab JM, Dubois JM, Sirodot M, Gaussorgues P, Robert D. Prone position in mechanically ventilated patients with severe acute respiratory failure. Am. J. Respir. Crit. Care Med 1997;155:473–478. [PubMed: 9032181]
22. Kim MJ, Hwang HJ, Song HH. A randomized trial on the effects of body positions on lung function with acute respiratory failure patients. Int. J. Nurs. Stud 2002;39:549–555. [PubMed: 11996875]

23. Petersson J, Sanchez-Crespo A, Larsson SA, Mure M. Physiological imaging of the lung: single-photon-emission computed tomography (SPECT). J. Appl. Physiol 2007;102:468–476. [PubMed: 16990505]
24. King GG, Eberl S, Salome CM, Meikle SR, Woolcock AJ. Airway closure measured by a Technegas bolus and SPECT. Am. J. Respir. Crit. Care Med 1997;155:682–688. [PubMed: 9032213]
25. King GG, Eberl S, Salome CM, Young IH, Woolcock AJ. Differences in airway closure between normal and asthmatic subjects measured by single-photon emission computed tomography and Technegas. Am. J. Respir. Crit. Care Med 1998;158:1900–1906. [PubMed: 9847284]
26. Fichele S, Woodhouse N, Swift AJ, Said Z, Paley MNJ, Kasuboski L, Mills GH, van Beek EJR, Wild JM. MRI of Helium-3 Gas in Healthy Lungs: Posture Related Variations of Alveolar Size. J. Magn. Reson. Imaging 2004;20:331–335. [PubMed: 15269962]
27. Musch G, Layfield JD, Harris RS, Melo MF, Winkler T, Callahan RJ, Fischman AJ, Venegas JG. Topographical distribution of pulmonary perfusion and ventilation, assessed by PET in supine and prone humans. J. Appl. Physiol 2002;93(5):1841–1851. [PubMed: 12381773]
28. Vidal Melo MF, Layfield D, Harris RS, ONeill K, Musch G, Richter T, Winkler T, Fischman AJ, Venegas JG. Quantification of Regional VentilationPerfusion Ratios with PET. J. Nucl. Med 2003;44:1982–1991. [PubMed: 14660725]
29. Jinkins JR, Dworkin JS, Green AC, Greenhalgh JF, Gianni M, Gelbien M, Wolf RB, Damadian J, Damadian RV. Upright, Weight-Bearing, Dynamic-Kinetic MRI of the Spine pMRI/kMRI. Rivista di Neuroradiologia 2002;15(1):333–356.
30. Jinkins JR. Acquired degenerative changes of the intervertebral segments at and suprajacent to the lumbosacral junction A radioanatomic analysis of the nondiscal structures of the spinal column and perispinal soft tissues. European Journal of Radiology 2004;50(1):134–158. [PubMed: 15081129]
31. Tsai LL, Mair RW, Li C-H, Rosen MS, Patz S, Walsworth RL. Posture-Dependent Human ^{3}He Lung Imaging in an Open Access MRI System: Initial Results. Acad. Radiol 2008;15(6):728–739. [PubMed: 18486009]
32. Hoffman EA. Effect of body orientation on regional lung expansion: a computed tomographic approach. J. Appl. Physiol 1985;59:468–480. [PubMed: 4030599]
33. Martin-Du Pan RC, Benoit R, Girardier L. The role of body position and gravity in the symptoms and treatment of various medical diseases. Swiss Med. Wkly 2004;134:543–551. [PubMed: 15551157]
34. Galvin I, Drummond GB, Nirmalan M. Distribution of blood flow and ventilation in the lung: gravity is not the only factor. Br. J. Anaesth 2007;98:420–428. [PubMed: 17347182]
35. Hopkins SR, Henderson AC, Levin DL, Yamada K, Arai T, Buxton RB, Prisk GK. Vertical gradients in regional lung density and perfusion in the supine human lung: the Slinky effect. J. Appl. Physiol 2007;103:240–248. [PubMed: 17395757]
36. Gattinoni L, Tognoni G, Pesenti A, Taccone P, Mascheroni D, Labarta V, Malacrida R, Di Giulio P, Fumagalli R, Pelosi P, Brazzi L, Latini R. Effect of prone positioning on the survival of patients with acute respiratory failure. N. Engl. J. Med 2001;345:568–573. [PubMed: 11529210]
37. Wang L-Y, Cerny FJ, Kufel TJ, Grant BJB. Simulated Obesity-Related Changes in Lung Volume Increases Airway Responsiveness in Lean, Nonasthmatic Subjects. Chest 2006;130:834–840. [PubMed: 16963683]
38. van Beek, EJR. Proc. Phelinet General Training School: Lung Imaging with Hyperpolarized Helium-3 Magnetic Resonance - from gas production to medical application. Paris, France: 2008 Jan 21–26. Lung Morphology and Function using CT and MRI.
39. Tseng CH, Wong GP, Pomeroy VR, Mair RW, Hinton DP, Hoffmann D, Stoner RE, Hersman FW, Cory DG, Walsworth RL. Low-field MRI of laser polarized noble gas. Phys. Rev. Lett 1998;81(17): 3785–3788. [PubMed: 11543589]
40. Wong GP, Tseng CH, Pomeroy VR, Mair RW, Hinton DP, Hoffmann D, Stoner RE, Hersman FW, Cory DG, Walsworth RL. A system for low field imaging of laser-polarized noble gas. J. Magn. Reson 1999;141(2):217–227. [PubMed: 10579945]
41. Parra-Robles J, Cross AR, Santyr GE. Theoretical signal-to-noise ratio and spatial resolution dependence on the magnetic field strength for hyperpolarized noble gas magnetic resonance imaging of human lungs. Med. Phys 2005;32(1):221–229. [PubMed: 15719973]

42. Mair RW, Hrovat MI, Patz S, Rosen MS, Ruset IC, Topulos GP, Tsai LL, Butler JP, Hersman FW, Walsworth RL. ^{3}He lung imaging in an open access, very-low-field human magnetic resonance imaging system. Magn. Reson. Med 2005;53(4):745–749. [PubMed: 15799045]
43. Ruset IC, Tsai LL, Mair RW, Patz S, Hrovat MI, Rosen MS, Muradian I, Ng J, Topulos GP, Butler JP, Walsworth RL, Hersman FW. A system for open-access He-3 human lung imaging at very low field. Concepts Magn. Reson. B - Magn. Reson. Eng 2006;29B(4):210–221.
44. Owers-Bradley JR, Fichele S, Bennattayalah A, McGloin CJ, Bowtell RW, Morgan PS, Moody AR. MR tagging of human lungs using hyperpolarized ^{3}He gas. J. Magn. Reson. Imaging 2003;17(1): 142–146. [PubMed: 12500284]
45. Durand E, Guillot G, Darrasse L, Tastevin G, Nacher PJ, Vignaud A, Vattolo D, Bittoun J. CPMG measurements and ultrafast imaging in human lungs with hyperpolarized helium-3 at low field (0.1 T). Magn. Reson. Med 2002;47(1):75–81. [PubMed: 11754445]
46. Venkatesh AK, Zhang AX, Mansour J, Kubatina L, Oh CH, Blasche G, Selim Unlu M, Balamore D, Jolesz FA, Goldberg BB, Albert MS. MRI of the lung gas-space at very low-field using hyperpolarized noble gases. Magn. Reson. Imaging 2003;21(7):773–776. [PubMed: 14559342]
47. Bidinosti CP, Choukeife J, Nacher PJ, Tastevin G. In vivo NMR of hyperpolarized ^{3}He in the human lung at very low magnetic fields. J. Magn. Reson 2003;162(1):122–132. [PubMed: 12762989]
48. Bidinosti CP, Choukeife J, Tastevin G, Vignaud A, Nacher PJ. MRI of the lung using hyperpolarized ^{3}He at very low magnetic field (3 mT). Magma 2004;16(6):255–258. [PubMed: 15029510]
49. Morgan, PS.; Conolly, S.; Makovski, A. Design of uniform field biplanar magnets; 5th Meeting of ISMRM; Canada. Vancouver; 1997. p. 1447
50. Gottardi G, Mesirca P, Agostini C, Remondini D, Bersani F. A four coil exposure system (tetracoil) producing a highly uniform magnetic field. Bioelectromagnetics 2003;24(2):125–133. [PubMed: 12524679]
51. Chia C-T, Wang Y-F. The magnetic field along the axis of a long finite solenoid. The Physics Teacher 2002;40(5):288–289.
52. Hoult DI, Lauterbur PC. The Sensitivity of the Zeugmatographic Experiment Involving Human Samples. J. Magn. Reson 1979;34(2):425–433.
53. Wild JM, Woodhouse N, Paley MNJ, Fichele S, Said Z, Kasoboski L, van Beek EJR. Comparison Between 2D and 3D Gradient-Echo Sequences for MRI of Human Lung Ventilation With Hyperpolarized ^{3}He. Magn. Reson. Med 2004;52(4):673–678. [PubMed: 15334590]
54. Kim YR, Rebro KJ, Schmainda KM. Water Exchange and Inflow Affect the Accuracy of T1-GRE Blood Volume Measurements: Implications for the Evaluation of Tumor Angiogenesis. Magn. Reson. Med 2002;47(6):1110–1120. [PubMed: 12111957]
55. Hoult DI, Richards RE. Signal-to-noise ratio of nuclear magnetic-resonance experiment. J. Magn. Reson 1976;24(1):71–85.
56. Callaghan, PT. Principles of nuclear magnetic resonance microscopy. Oxford [England] New York: Clarendon Press; Oxford University Press; 1991.
57. Darrasse L, Guillot G, Nacher P-J, Tastevin G. Low-field He-3 nuclear magnetic resonance in human lungs. Comptes Rendus De L Academie Des Sciences Serie Ii Fascicule B-Mecanique Physique Chimie Astronomie 1997;324(11):691–700.
58. Saam B, Happer W, Middleton H. Nuclear relaxation of ^{3}He in the presence of O_2. Phys. Rev. A 1995;52(1):862–865. [PubMed: 9912313]
59. Vignaud A, Maitre X, Guillot G, Durand E, de Rochefort L, Robert P, Vives V, Santus R, Darrasse L. Magnetic susceptibility matching at the air-tissue interface in rat lung by using a superparamagnetic intravascular contrast agent: Influence on transverse relaxation time of hyperpolarized helium-3. Magn. Reson. Med 2005;54(1):28–33. [PubMed: 15968677]
60. Claasen-Vujcic T, Borsboom HM, Gaykerna HJG, Mehlkopf T. Transverse Low-Field RF Coils in MRI. Magn. Reson. Med 1996;36:111–116. [PubMed: 8795029]
61. Lurie DJ, Li H, Petryakov S, Zweier JL. Development of a PEDRI Free-Radical Imager Using a 0.38 T Clinical MRI System. Magn. Reson. Med 2002;47:181–186. [PubMed: 11754457]
62. Mohoric A, Planinsic G, Kos M, Duh A, Stepisnik J. Magnetic Resonance Imaging System Based on Earths Magnetic Field. Inst. Sci. Tech 2004;32(6):655–667.

63. Yablonskiy DA, Sukstanskii AL, Ackerman JJH. Image artifacts in very low magnetic field MRI: The role of concomitant gradients. J. Magn. Reson 2005;174(2):279–286. [PubMed: 15862245]

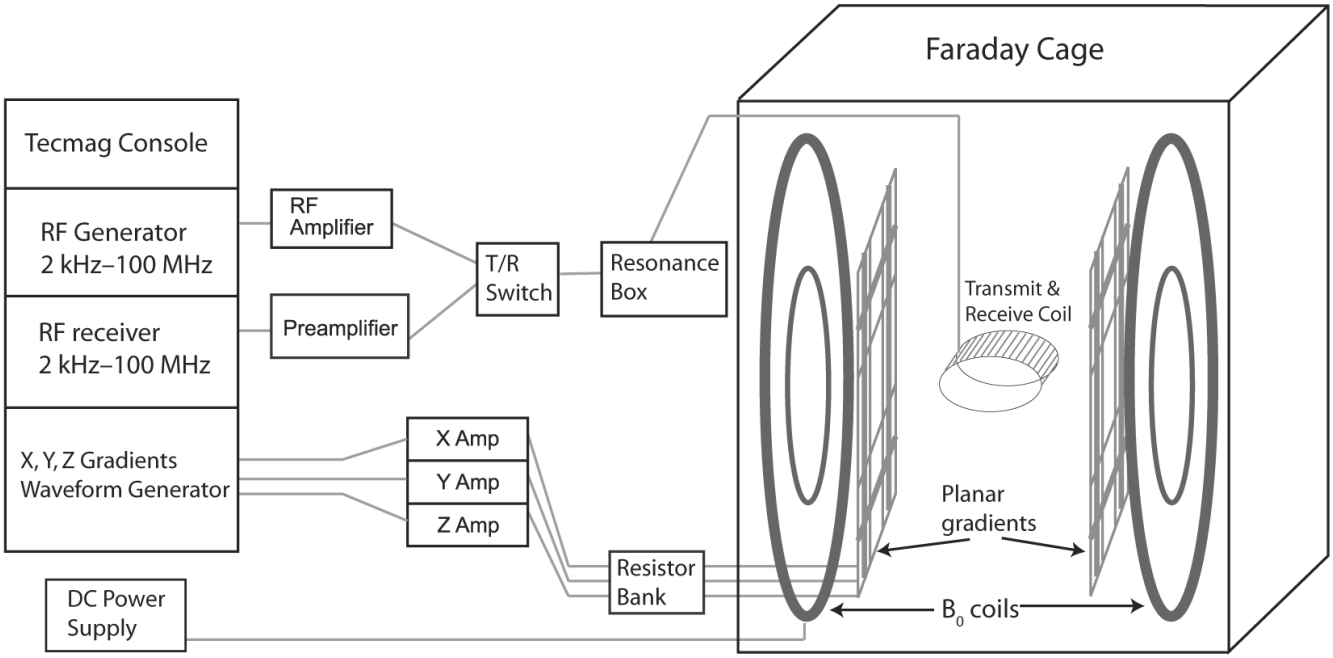

Fig. 1.

Schematic of the open-access human MRI system. The major components include an MRI research console (left), electronics components for RF and gradient pulse generation and B_0 control (center), and the B_0, gradient and B_1 coils, located inside an RF-shielding Faraday cage (right). The resonance box, T/R switch and preamplifier are located inside the Faraday cage, but are drawn as shown for clarity.

Fig. 2.
Left: The B_0 and gradient coils mounted on the aluminum flange. The arrows point to the outer and inner B_0 coils. The other circular coils are the *z* gradient coils, while the rectangular coils are the *x* and *y* gradient coils. Right: A view of the imaging region with the imaging axes defined. The *x* axis points out of the page.

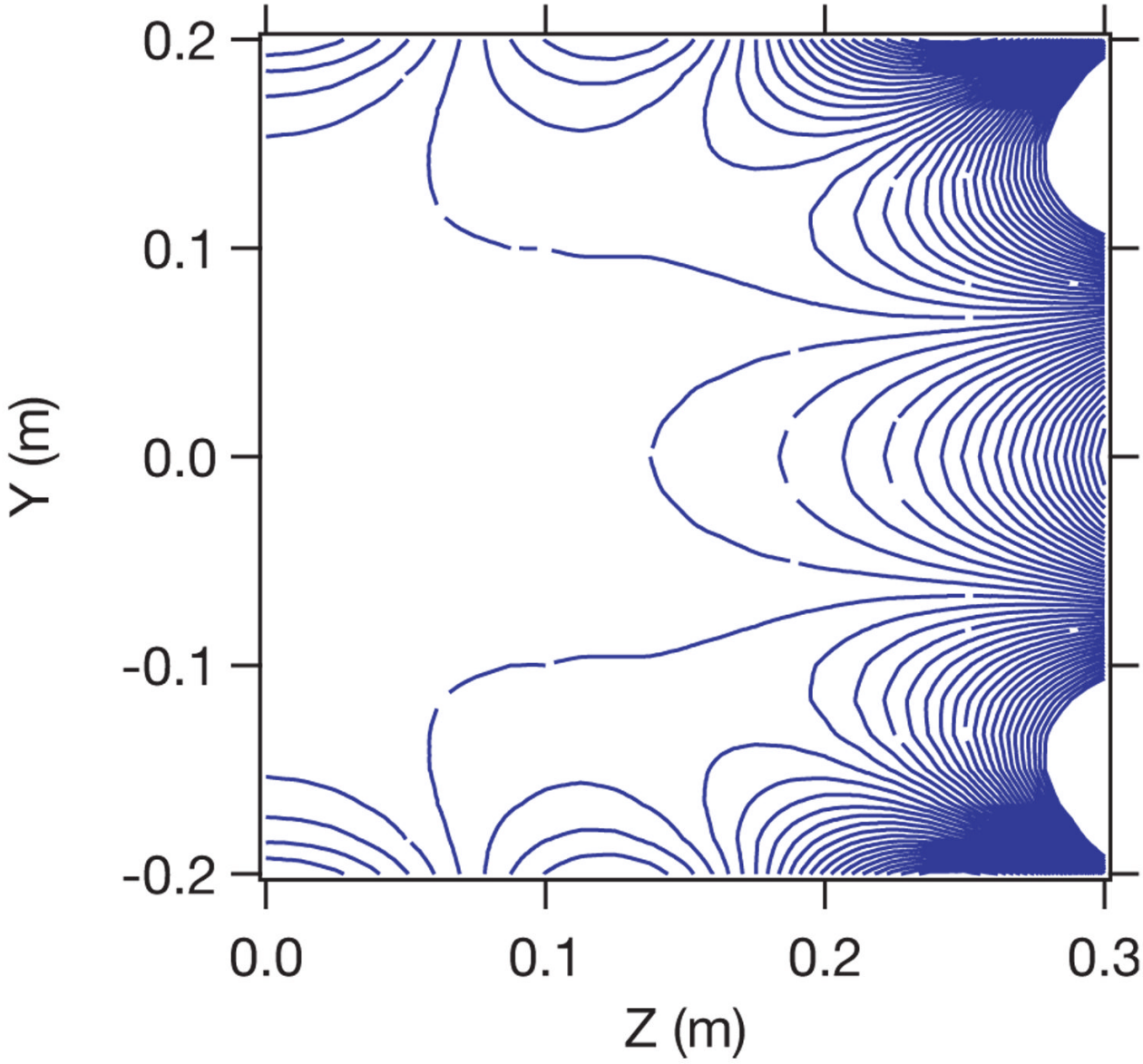

Fig. 3.

Calculated plot of B_0 homogeneity for the biplanar, four-coil arrangement. The ordinate represents the *y* axis of the imager and intersects the center of the magnet at zero. The abscissa represents the distance from the central *y* axis, along *z*; thus, one half of the region of interest is shown. Each contour line is a 25 ppm B_z deviation from the center B_0. The design target DSV is 0.4 m.

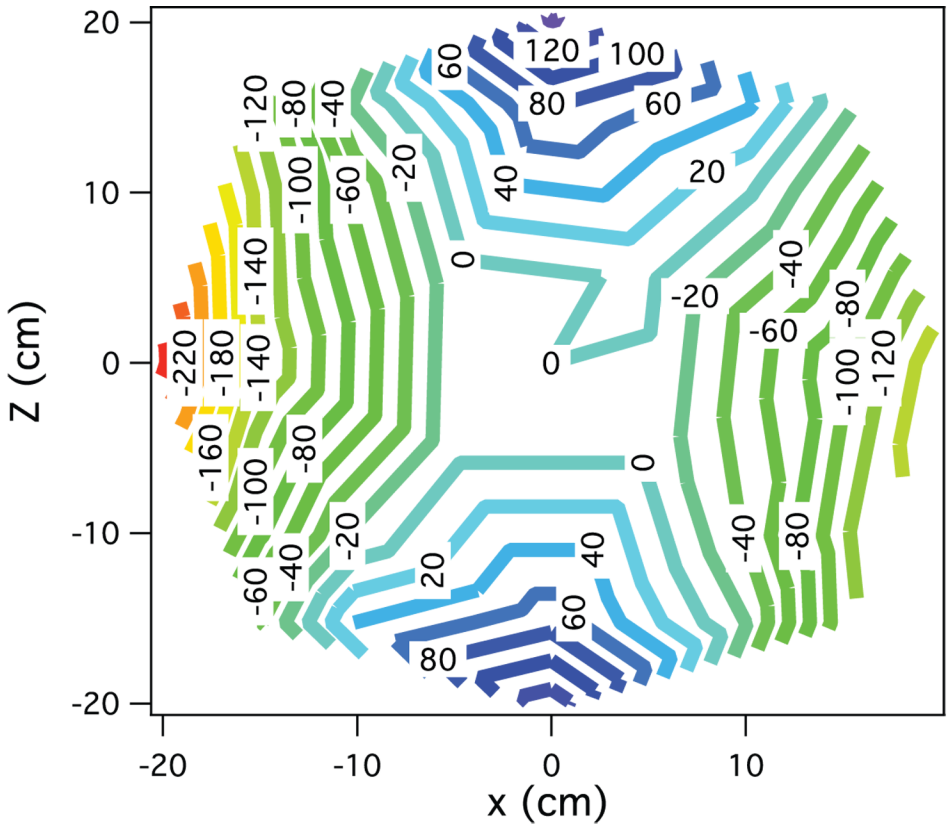

Fig. 4.

B_0 field map for the *x*-*z* plane, obtained after optimization of passive shim placement. Contours indicate deviation of ^{1}H NMR frequency in Hz from the zero–center frequency is 210 kHz. Across a human lung of width ~ 25 cm, $\nu_0 \sim \pm 80$ Hz, which implies the B_0 homogeneity $\Delta B_0 \sim \pm 0.02$ G or about 350 ppm.

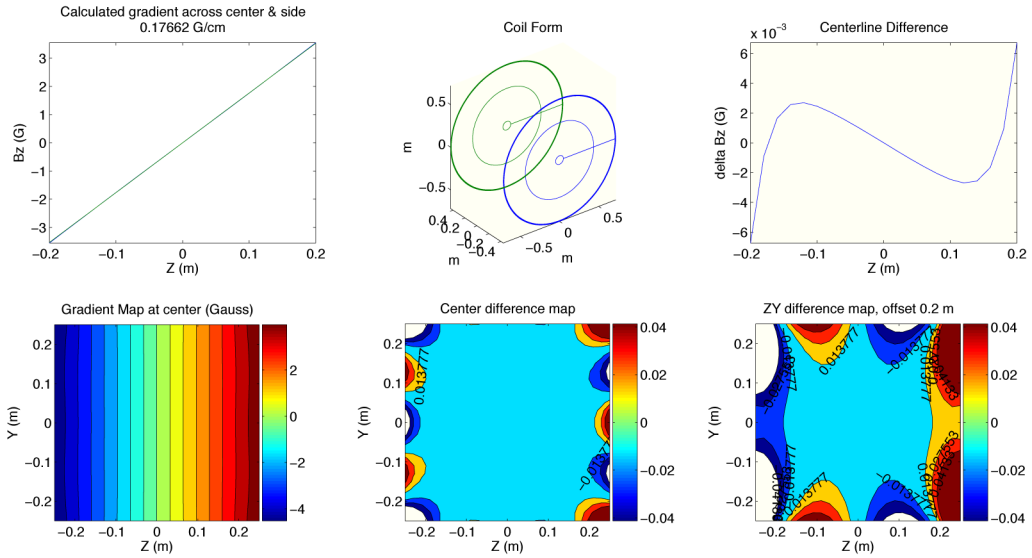

Fig. 5.

Sample output of the MATLAB gradient coil optimization routine, in this case for a *z* gradient coil form. The program determines the magnetic field strength and produces a predicted gradient field map as well as plots of the deviation from an ideal gradient for the given coil design under consideration.

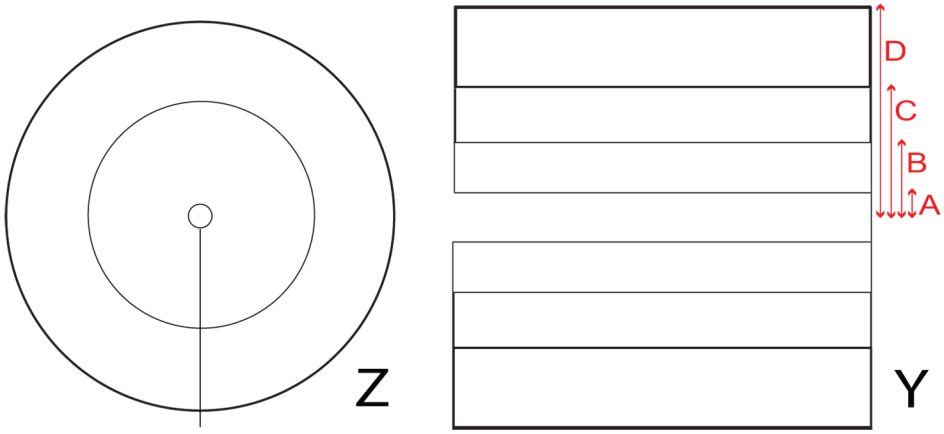

Fig. 6.

Left: A diagram of the *z* gradient loop pattern, showing the inner, middle, and outer sections. The current flow is in the same direction for all loops. Right: A diagram of the *y* gradient loop pattern, with thicker lines indicating more turns. The current flow is in the same direction for all loops. The loop dimensions for the *y* gradient pattern are denoted by letters on the figure: A = 8.05 cm, B = 24.75 cm, C = 45.9, 46.4, and 46.9 cm, D = 68.0, 68.5, 69.0, 69.5 and 70.0 cm. For the *x* gradient pattern, the corresponding dimensions are: A = 8.55 cm, B = 26.4 cm, C = 47.5, 48.0, and 48.5 cm, D = 68.0, 68.5, 69.0, 69.5 and 70.0 cm

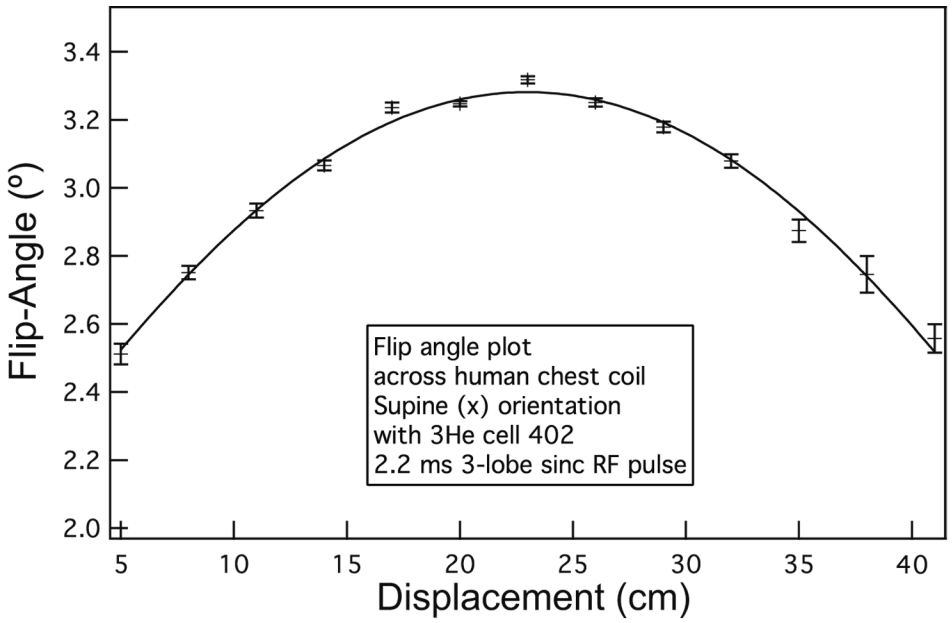

Fig. 7.

Measured ^{3}He flip-angle versus position along the center axis of the human chest coil oriented for supine lung imaging (i.e., along the imager's *x* axis). Flip-angle calibrations were performed on hyperpolarized ^{3}He cell #402 which had a 3 cm width along the *x* axis. Displacement is measured from one end of the chest coil. The solid curve is a fit of the data to the function describing the B_1 field created by an ideal finite solenoid.

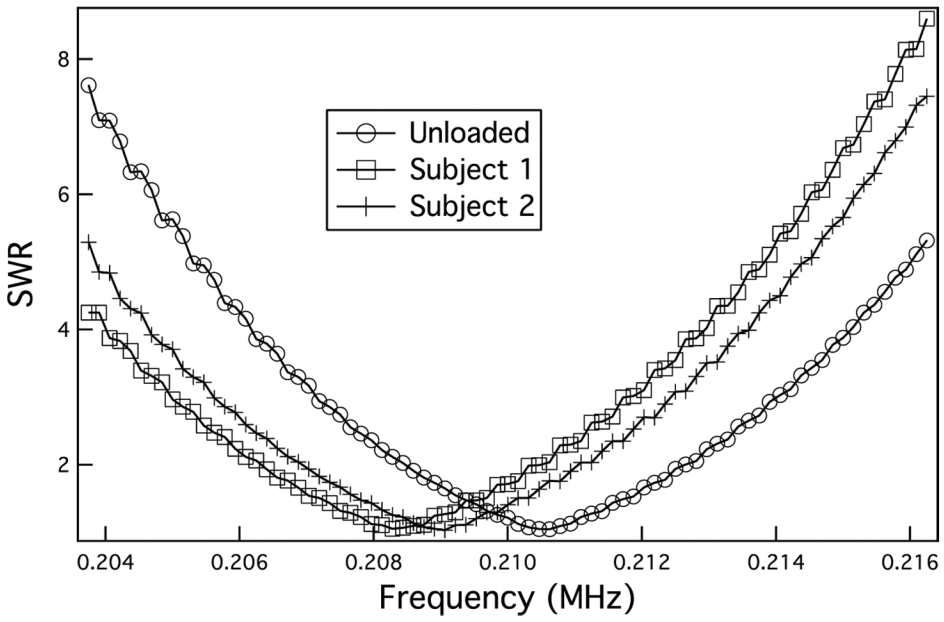

Fig. 8.
Measured SWR as a function of frequency for the human chest coil unloaded as well as loaded by two different human subjects weighing between 60–80 kg.

Fig. 9.
The OAI with human subjects in the supine position (left) and the upright position (right).

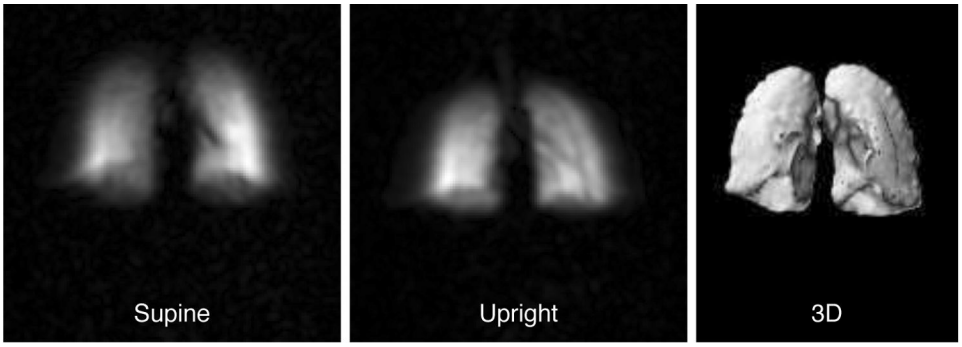

Fig. 10.

Demonstration of human lung imaging with the open-access imager. All images shown here are from the same subject. Left: 2D projection ^{3}He MR image with the subject supine. From [31]. Center: 2D projection ^{3}He MR image with the subject vertical. From [31]. Right: 3D reconstructed ^{3}He MR image with the subject supine. The anterior face of the lungs is shown in all images, revealing the cardiac profile. Imaging parameters: $B_0 = 65$ G, $\nu_0 = 210$ kHz, FOV = 50 cm, no signal averaging, $\theta = 4.1°$, $T_R = 86$ ms, $T_E = 29$ ms. For 2D images, dataset was 128 × 64, zero-filled to 128 × 128, total scan time ~ 4 s. For the 3D image, dataset was 128 × 64 × 6, zero-filled to 128 × 128 × 8, slice thickness = 1.5 cm, total scan time ~ 33 s.

Table 1

Design and circuit characteristics of three commonly used RF coils on the OAI. Length and diameter in cm. L inductance in μH, R resistance in Ω, C_T and C_M tuning and matching capacitance in pF for a conventional series-resonated circuit.

Coil Name	Use	Length	Diam.	Turns	L	R	C_T	C_M	Q
Coil A	^{1}H NMR	6	4	50	210	15	900	540	60
25 cm Coil	^{1}H MRI	30	25	64	610	24	58	320	30
Human Coil	All ^{3}He MRI	46	52	44	800	15	0	488	30

Table 2

A comparison of T_2^* contributions at 1.5 T and 6.5 mT, along with the typical total value of T_2^*. A value of T_2 = 10 s is used in both cases [57], while $T_{2,in} \sim 0.143$ s is used for the 1.5 T case [41]. ^{3}He T_2^* is based on our measured $\Delta B_0 \simeq$ 0.04 G. Inverse values (relaxation rates) are given in square brackets.

T_2^* Contribution	B_0 = 1.5 T $\Delta B_0 \sim$ 0.1 G	B_0 = 6.5 mT $\Delta B_0 \sim$ 0.4 G
T_2 (s) [R_2 (s^{-1})]	10 [0.1]	10 [0.1]
$T_{2,in}$ (s) [$R_{2,in}$ (s^{-1})]	0.143 [6.99]	0.016 [62.5]
$T_{2,sus}$ (s) [$R_{2,sus}$ (s^{-1})]	0.0046 [217.4]	1.10 [0.91]
$T_{2,diff}$ (s) [$R_{2,diff}$ (s^{-1})]	0.031 [32.3]	1672 [0.0006]
$T_{2,grad}$ (s) [$R_{2,grad}$ (s^{-1})]	0.512 [1.95]	3.6 [0.28]
T_2^* (ms) [R_2^* (s^{-1})]	3.8 [263.1]	15.6 [64.1]